communications earth & environment

A Nature Portfolio journal

Article

https://doi.org/10.1038/s43247-025-02792-2

The key role of the Southern Annular Mode during the sea-ice maximum for Antarctic sea ice and its recent loss

Check for updates

Chloe L. Boehm [1] ✉, **David W. J. Thompson** [1,2] **& Edward Blanchard-Wrigglesworth** [3]

Antarctic sea ice exhibits considerable interannual variability and has experienced unprecedented decline over the past decade. Here we provide observational insights into the role of the Southern Annular Mode in driving such variations in Antarctic sea-ice area. The influence of the Southern Annular Mode on Antarctic sea-ice area exhibits more pronounced seasonality than indicated in previous work. Positive anomalies in the Southern Annular Mode lead to decreases in sea-ice area during the seasonal sea-ice maximum, but vice versa during the sea-ice minimum. Variations in Southern Annular Mode during the sea-ice maximum also have an outsized influence on annual-mean changes in sea-ice area, since the seasonally-varying persistence and shortwave effects of sea-ice anomalies peak during the following months. It is argued that a notable fraction of the dramatic losses in annual-mean sea-ice area over the past decade can be traced to variations in the Southern Annular Mode during the sea-ice maximum.

Southern Hemisphere-mean sea-ice area (SIA) exhibited small increases from the early 1980s through 2015, but has decreased abruptly since, setting record negative anomalies in November 2016 and July 2023[1–5] (Fig. 1a). In total, annual mean Antarctic sea-ice extent decreased by roughly 2.5 million square kilometers between 2015 and 2023.

Various physical factors have been linked to both the weak increases in Antarctic sea ice between 1980 and 2015 and the dramatic losses thereafter (e.g., see discussion in ref. 6). The early sea-ice increases have been linked to tropical phenomena such as the El Niño-Southern Oscillation (ENSO)[7–12]; freshening of the Southern Ocean via ice shelf melt and changes in precipitation/evaporation[13–18]; Southern Ocean cooling[19,20]; sea-ice drift[21]; changes in the surface flow linked to ozone depletion[22,23]; and variations in the atmospheric flow over the Southern Ocean[19,24–30]. The recent declines have likewise been linked to a wide range of atmospheric and oceanic processes. These include wavelike variability in the atmospheric flow[31,32], the Indian Ocean Dipole[33], changes in upper-ocean heat content[34–38], and—as is the focus here–changes in the Southern Annular Mode (SAM) [3,31,35,39–41].

The SAM is characterized by variations in the strength of the westerly winds over the Southern Ocean (e.g., ref. 42). In general, the contribution of the SAM to *regionally-varying* changes in Antarctic sea ice is robust[23,26,43,44] but its contribution to *hemispheric-mean* changes in sea ice is less clear, in large part because its signature on Antarctic sea ice varies in sign from one sector of the hemisphere to the next (e.g., ref. 26). Some studies have argued that the SAM contributed to the increases in Antarctic SIA from the 1980s–2000s[22,23,45,46], whereas others have argued that the SAM had little influence on both the weak hemispheric-mean increases in sea ice through the 2000s[44,47,48] and the more pronounced decreases in Antarctic SIA since ~2015[44]. To date, variations in the SAM have not been conclusively linked to the large drops in Antarctic SIA centered around 2016/2017 and 2022/2023. As noted in Polvani et al.[44]: "the SAM/sea-ice extent relationship is tenuous".

Here, we provide observational insights into the influence of the SAM on variations in hemispheric-mean Antarctic sea ice, especially over the past decade. We reveal that by far the largest influence of the SAM on annual-mean changes in SIA arises not from contemporaneous variations in the SAM, nor from variations in the SAM during the summer months when the effects of ozone depletion on the surface circulation are most clear. Rather, we demonstrate that the most pronounced influence of the SAM on annual-mean SIA arises from variations in the SAM during the sea-ice maximum. The pronounced influence of the SAM on annual-mean SIA arises from a combination of the large contemporaneous relationships between the SAM and SIA during the sea-ice maximum, and the pronounced persistence of the sea-ice field during the ensuing months. We begin our analysis by exploring the lagged relationships between the SAM and SIA as a function of season.

[1]Department of Atmospheric Sciences, Colorado State University, Fort Collins, CO, USA. [2]School of Environmental Sciences, University of East Anglia, Norwich, UK. [3]Department of Atmospheric and Climate Science, University of Washington, Seattle, WA, USA. ✉e-mail: chloe.boehm@colostate.edu

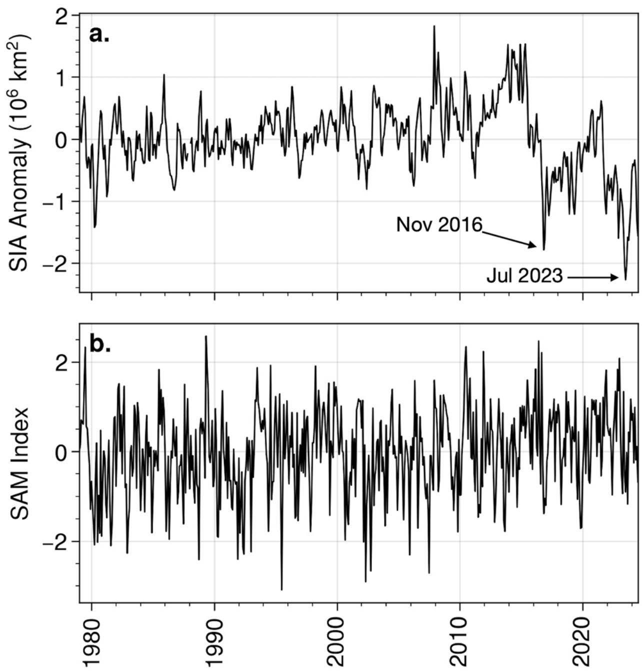

Fig. 1 | Observed time series of Antarctic sea-ice area and the Southern Annular Mode. Observed monthly-mean values of **a** Antarctic sea-ice area anomalies (SIA) and **b** the Southern Annular Mode (SAM). The time series are deseasonalized but not detrended. Months with record negative SIA anomalies are denoted on (**a**).

Results

Seasonality of the influence of the SAM on Southern Hemisphere SIA

The observational analyses are based on monthly gridded sea-ice concentration data, radiative flux data, wind data, and sea surface temperature data from satellite and reanalysis products (Methods). The time series of the SAM is defined as the leading principal component time series of monthly-mean 700 mb height anomalies south of 20°S (Methods). By definition, positive values of the index correspond to stronger-than-normal westerlies over the Southern Ocean, and vice versa. Analyses of sea ice and atmospheric data are based on the period January 1979 to July 2024; analyses of radiative flux data are based on the period March 2000 to July 2024. Unless otherwise noted, the long-term mean seasonal cycles and trends are removed from the data before performing the analyses. Details of the analysis procedure and data sources are provided in the Methods section.

We focus on the seasonally varying and lagged signature of the SAM in the Southern Hemisphere (SH) SIA. The SAM is key for Antarctic climate for a range of reasons: (1) It is the most prominent pattern of internal atmospheric variability in the mid-high latitude SH atmospheric circulation and thus accounts for a large fraction of the variance in the surface flow around Antarctica[42]; (2) It accounts for the majority of the SH circulation response to both stratospheric ozone depletion[49,50] and increasing greenhouse gases[51,52]; and (3) It accounts for a notable component of the SH response to ENSO, especially in summer[53].

To set the stage, Fig. 1a, b show the SH SIA and SAM indices as a function of month. As noted in the Introduction, SH mean SIA increased weakly through the mid-2010s and then dropped markedly after 2015, with record negative anomalies reported in 2016 and 2023[1,2,4] (Fig. 1a). The SAM index exhibits considerable variability from 1 month to the next but has also exhibited a weak positive trend throughout the period of record (Fig. 1b). The positive trend is most clear during the summer months and over the period of largest ozone losses through ~2000[50,54–56].

From Fig. 1a, it is visually apparent that SH SIA exhibits notable persistence for up to a few months (see also refs. 57–60), particularly over the past decade[61]. Figure 2a probes this persistence as a function of season. The first row shows the auto-regression of SIA during January, i.e., it shows SIA in units km^2 at the lags indicated on the x-axis regressed onto standardized values of SIA during January. Subsequent rows show analogous lag results based on standardized values of SIA for the months indicated on the y-axis. For example, results at lag zero in the October row indicate the regression of October values of SIA onto standardized October values of SIA; results at lag seven in the October row indicate the regression of May values of SIA (during the following calendar year) onto standardized October values of SIA; etc. Note that the lag zero results are equivalent to the year-to-year standard deviation of SH mean SIA time series for the months indicated on the y-axis. The results in Fig. 2c show the climatological-mean seasonal cycle of SIA as a point of reference for interpreting the seasonal cycle in the persistence. Corresponding correlations for Fig. 2a, b are shown in Supplementary Fig. 1, and hatching indicates regions where the correlations exceed the 95% level (Methods).

The results highlight the considerable persistence of SIA from 1 month to the next, with sea-ice anomalies persisting for several months during all times of the year[57–60]. They also highlight a unique pattern of reemergence in sea-ice anomalies that is most clear after the sea-ice maximum in September and October. Sea-ice anomalies during the sea-ice maximum persist for several months, reach a minimum in the following summer season (i.e., around lags 4–5, which correspond to January–February), and then remerge during the following season of sea-ice growth (i.e., around lags 7–8, which correspond to the following April–May). The sea-ice anomaly reemergence mechanism was first described for Arctic sea ice[62]; Fig. 2a indicates it also emerges in the Antarctic which is consistent with previous work (e.g., ref. 57). The reemergence of SIA anomalies from spring to the following autumn has been linked to oceanic processes[36,57–60,63,64] and is reminiscent of that found in association with extratropical SSTs (e.g., ref. 65). The reemergence is most clear following the sea-ice maximum and gives rise to significant persistence in the SIA field through the following winter (i.e., hatching indicates significance at the 95% confidence level; see also ref. 36).

Figure 2b explores the corresponding seasonally varying covariability between SIA and the SAM index. In this case, the first row shows SIA in units km^2 at the lags indicated on the x-axis regressed onto standardized values of the SAM during January; subsequent rows show analogous results for standardized values of the SAM during the months indicated on the y-axis. For example, results at lag seven in the October row indicate the regression of May values of SIA (during the following calendar year) onto standardized October values of the SAM, etc. Blue shading indicates increases in sea ice, and vice versa.

The results in Fig. 2b highlight two key aspects of the relationships between the SAM and hemispheric mean SIA that have not been widely appreciated in previous work:

1. The sign of the linkages between SIA and the SAM change from one season to the next. The regressions between the SAM and SIA are positive (that is, the positive polarity of the SAM gives rise to increases in SIA) during the annual sea-ice minimum between February and April, but negative during the annual sea-ice maximum between August and November. The in-phase relationship between the SAM and SIA during the annual sea-ice minimum is consistent with the sign of the relationships reported in Doddridge and Marshall (2017)[23] and Polvani et al.[44]. The out-of-phase relationship between SIA and the SAM during the annual sea-ice maximum is not expected based on previous work. Simpkins et al.[26] highlight regional decreases in sea ice associated with the SAM during September, October, and November, but they do not probe the corresponding changes in hemispheric mean SIA or the results as a function of lag. Holland et al.[64] demonstrate seasonally-varying lagged relationships between sea ice and the Amundsen Sea Low, but do not consider the hemispheric-mean impacts of the SAM.
2. Consistent with the persistence in the sea-ice field, the SAM-induced changes in sea ice persist for months after the largest anomalies in the circulation. In the case of the sea-ice maximum centered around

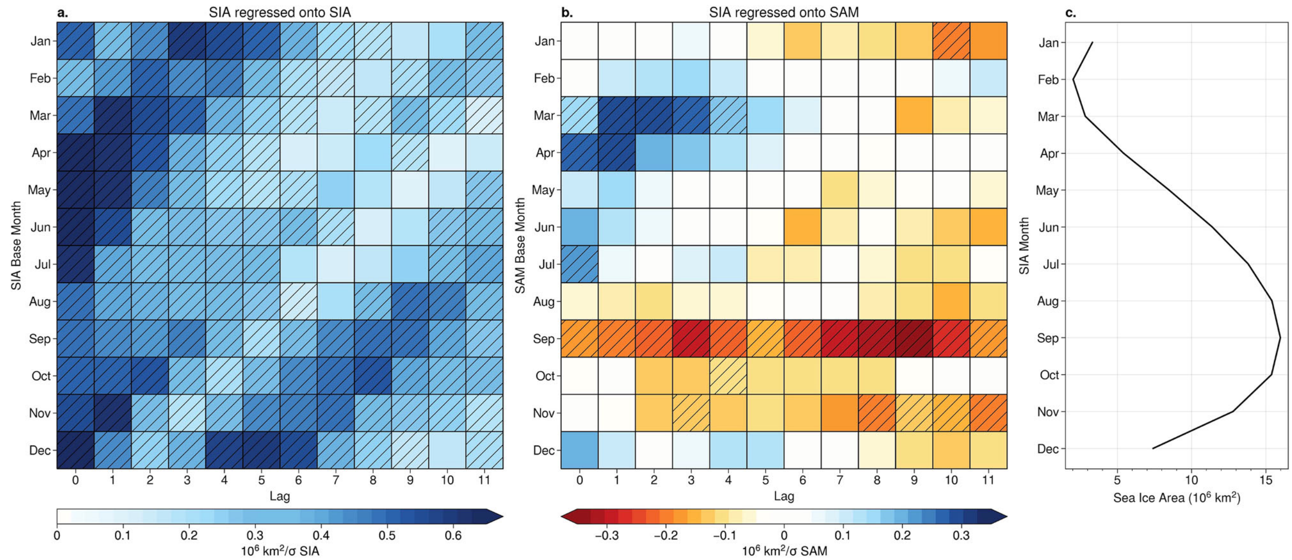

Fig. 2 | Seasonality of Antarctic sea ice and its relationship with the Southern Annular Mode. The regression of monthly-mean values of Southern Hemisphere-mean sea-ice area (SIA) regressed onto standardized values of **a** SIA and **b** the Southern Annular Mode (SAM) index. The months on the *y*-axis indicate the month used as a basis for the regression; the values on the *x*-axis indicate the lag with respect to the basis month. For example, the first row in (**b**) shows SIA in units km^2 at lags indicated on the *x*-axis regressed onto standardized values of the SAM index during January. All data used in (**a**, **b**) are detrended with respect to the long-term mean climatology. **c** Shows the climatological seasonal cycle of Antarctic SIA. Hatching indicates regressions that are statistically significant at the 95% confidence interval. See text for details.

September, the positive polarity of the SAM leads to decreases in SIA that last through the following fall and winter seasons, up to 11 months in the future. The regression coefficients are statistically significant for lags up to 3–4 months following the sea-ice minimum centered around March, and for lags up to 11 months following the sea-ice maximum during September. Notably, the relationship between the SAM and lagged SIA is insignificant during most other times of the year.

The top row in Fig. 3 shows the spatially varying signatures of the sea-ice anomalies that underlie the hemispheric mean results in the September row of Fig. 2b. Figure 3a–d show September, November, January, and March sea-ice anomalies regressed on September values of the SAM index; the vectors in Fig. 3a show the September near-surface wind anomalies regressed onto September values of the SAM index for context. Blue shading again indicates increases in sea ice, and vice versa. The area averages of the results in Fig. 3a–d are equal to the results in the September row of Fig. 2b. The climatological ice edge is indicated by the solid black contour.

Circulation anomalies associated with the positive polarity of the SAM are dominated by a zonally-symmetric strengthening of the circumpolar westerlies around Antarctica juxtaposed with poleward wind anomalies upstream of the Antarctic peninsula (vectors in Fig. 3a). The largest contemporaneous sea-ice anomalies arise along the equatorward edge of the sea-ice cover (shading in Fig. 3a) and are largely consistent with the signature of the SAM in the wind field, i.e., the most prominent regions of low sea ice (red shading) arise along ~60°S and in regions to the north of the Ross, Weddell and Davis Seas where the near-surface flow is anomalously southward. When summed over the hemisphere, the regions of sea-ice losses exceed those of sea-ice increases and thus September variations in the SAM are associated with a net decrease in SIA during September (Fig. 2b). At increasingly longer lags, the decreases in sea ice found during September follow the seasonal cycle of the sea-ice edge, with sea-ice decreases retreating to the periphery of Antarctica during the summer (Fig. 3b–d).

Supplementary Fig. 2 shows companion results for variations in the SAM during the annual sea-ice minimum centered around March. In this case, the SAM-related wind anomalies have a northward component over the Ross, Davis, and Weddell Seas that is consistent with cold temperature advection in these regions. The most prominent northward anomalies overlie regions of positive sea-ice anomalies that give rise to the increases in SIA in the March row of Fig. 2b. The sea-ice anomalies initiated during the sea-ice minimum persist along the sea-ice edge as it expands during winter, albeit as also indicated in Fig. 2b, their amplitude weakens through the following spring.

What drives the persistence of the sea-ice anomalies associated with the SAM? A variety of factors give rise to memory in SH sea ice, including upper ocean heat content and radiative feedbacks[36,57,59,60]. The results in the bottom two rows of Fig. 3 suggest clear-sky shortwave (SW) feedbacks play a key role in maintaining the SAM-induced anomalies in the sea-ice field. The middle row in Fig. 3 shows clear-sky SW fluxes from the Clouds and the Earth's Radiant Energy System (CERES) data product[66] regressed onto September values of the SAM index; the bottom row shows the same results but for CERES SW cloud radiative effects (CRE). Red values indicate anomalous fluxes into the surface. The regions of persistent sea-ice decreases (top row) are overlaid by regions of clear-sky SW flux anomalies into the surface (middle row). The anomalous clear-sky SW fluxes are consistent with changes in surface albedo associated with the sea-ice anomalies and act to support the anomalous changes in surface temperature associated with the SAM-driven changes in sea ice. The SW CRE acts in the opposite sense: Regions of sea-ice loss (top row) are overlaid by regions of anomalous upward SW CRE (bottom row). While the SW CRE anomalies counteract the clear-sky SW anomalies, the latter are substantially larger, thus dominating the SW response to the SAM-driven changes in sea ice.

The factors that give rise to the long persistence of winter SAM-induced anomalies in SH SIA are further probed in Fig. 4. The solid black line shows the regression of SH-mean SIA regressed onto September values of the SAM as a function of lag, i.e., the results are identical to the September results from Fig. 2b. Note that the amplitudes for the SH-mean SIA in Fig. 4 are given as 10^7 km^2 to align with the range of the *y*-axis. The solid blue and gray lines show companion results for the SW clear-sky and SW CRE, respectively, where the fluxes are averaged over regions where the sea-ice concentration anomalies for the corresponding month are negative. For example, the values indicated by the blue line for November correspond to the clear-sky SW fluxes from Fig. 3f averaged over regions where the sea-ice concentration anomalies are negative in Fig. 3b. We focus on regions where the concentrations are negative so that the results indicate radiative flux

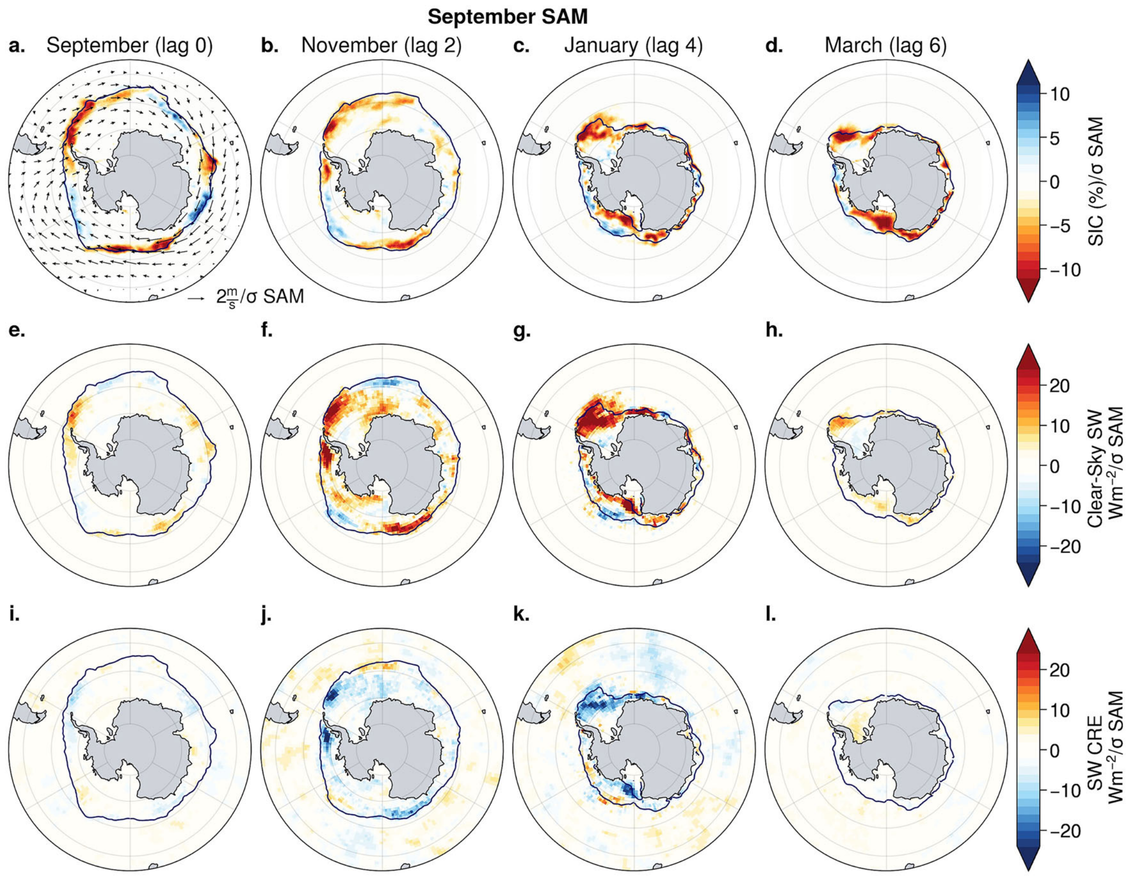

Fig. 3 | Regressions onto standardized September values of the Southern Annular Mode index. a–d Sea-ice concentration (SIC) for the indicated months regressed onto standardized September values of the Southern Annular Mode (SAM) index. Vectors in (**a**) show results for September 10-m winds. **e–h** As in (**a–d**) but for clear-sky surface shortwave (SW) fluxes regressed onto standardized September values of the SAM index. **i–l** As in (**a–d**) but for cloudy surface SW fluxes (SW cloud radiative effects (CRE)) regressed onto standardized September values of the SAM index. Black contours indicate where the climatological-mean monthly mean sea-ice concentration is at least 15%. Data are detrended with respect to the long-term mean climatology. Flux anomalies are positive downward and are based on the period 2000–2024.

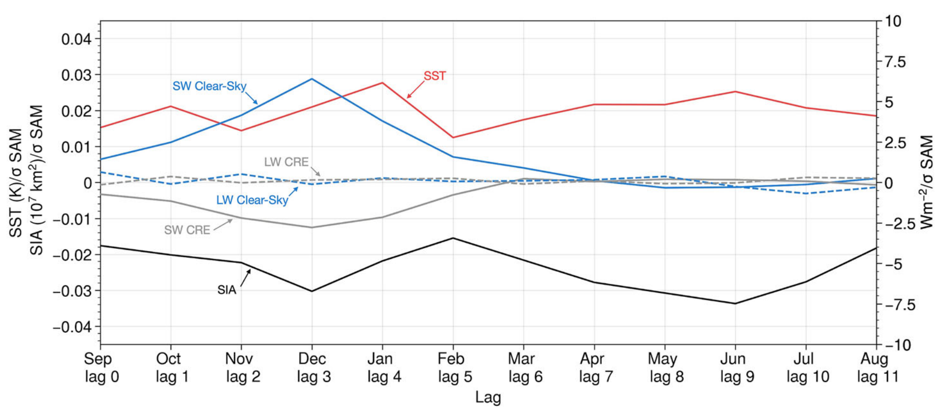

Fig. 4 | Regressions onto standardized September values of the Southern Annular Mode index as a function of lag. Black line: The regression of Southern Hemisphere-mean sea-ice area (SIA) as a function of lag onto standardized September values of the Southern Annular Mode (SAM) index. Gray and blue solid lines: As in the black line, but for shortwave (SW) cloud radiative effects (CRE) and SW clear-sky fluxes, respectively. Gray and blue dashed lines: As in the black line, but for longwave (LW) CRE and clear-sky fluxes, respectively. Red line: As in the black line, but for sea surface temperatures (SST). Amplitudes for all fluxes are given on the right axis; amplitudes for SST anomalies and SIA anomalies are indicated on the left axis. The fluxes and SST anomalies are averaged over regions where the sea-ice concentration anomalies for the corresponding month are negative. All data are detrended with respect to the long-term mean climatology. Fluxes are given over the period 2000–2024. See text for details.

Fig. 5 | Quantifying the seasonal relationships between sea-ice area and the Southern Annular Mode. a The regression of annual-mean sea-ice area (SIA) anomalies onto monthly values of the Southern Annular Mode (SAM) index, where the annual means are formed from the 12 month period starting on the month indicated on the *x*-axis. For example, results for September indicate September–August (during the following year) mean values of SIA regressed onto September values of the SAM index, etc. **b** Monthly-varying values of monthly SIA anomalies discretized by the value of the SAM index during September (colors). Years with anomalously high or low SIA are denoted on the plot. September SAM indices are standardized, and only years with September SAM index values exceeding ± 1 standard deviation are shown. Figure concept inspired by Doddridge and Marshall (2017)[23]. All data are detrended with respect to the long-term mean climatology.

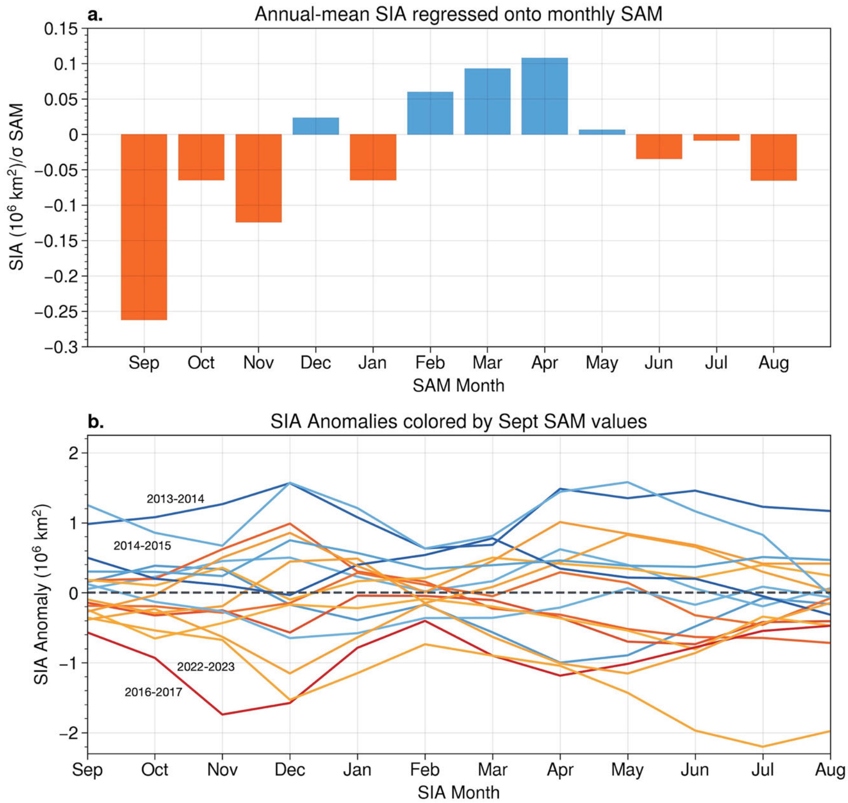

anomalies over regions of sea-ice loss. Nevertheless, similar results are derived when the fluxes are averaged over regions of both positive and negative sea-ice anomalies. As evidenced in Fig. 4, the clear-sky SW fluxes act to warm the surface and thus support the persistence in sea-ice loss, whereas the SW CRE act to cool the surface. The corresponding changes in the longwave (LW) fluxes (dashed blue and gray lines) are weak during all lags. Note that the small changes in LW CRE suggest that the changes in SW CRE are driven by variations in low-level clouds that have a weak signature in the LW since they are close to the surface temperature. The implied changes in low-level clouds over regions of sea-ice loss are reminiscent of similar relationships between regions of open water and low-level clouds over the Arctic[67].

The SW flux anomalies in Fig. 4 decrease rapidly after roughly month six with the onset of the following winter. The persistence of the sea-ice anomalies beyond March can be understood from the thermal inertia of the ocean mixed layer. The solid red line in Fig. 4 is constructed in the same manner as the flux results, but for anomalies in sea-surface temperature (SST) from the Hadley Centre Sea Ice and Sea Surface Temperature data set[68]. Ocean heat content from the Argo data product does not consistently sample regions poleward of 65°S[69], thus we use SSTs over regions of sea-ice anomalies as a proxy for heat storage in the ocean mixed layer[43,63]. Periods of low sea ice during September are followed by positive SST anomalies that peak in summer and persist through the following fall and winter months. The persistence of the SST anomalies is not due to shared low-frequency variability in the SAM and SST data: Both datasets are detrended before the analyses, and we confirmed that the regression coefficients drop to zero at negative lags. As noted earlier, the persistence in ocean heat content is also thought to underlie the reemergence of SH sea-ice anomalies[36,57–60,63,64].

Why is the amplitude and persistence of the signature of the SAM in SIA so much more pronounced after September than the surrounding months? The persistence in SIA can not be traced to persistence in the SAM itself—there is little memory inherent in the SAM index from one month to the next, particularly following the sea-ice maximum (Supplementary Fig. 3). Presumably, the analysis is not sensitive to the exact days used in the analysis, and similar results would emerge from analyses based on, say, the last weeks of August through the first weeks of October. Nevertheless, it is notable that results based on July and August are marked by much weaker SW clear-sky fluxes at positive lag, which suggests those months are less prominent since the SW fluxes - and thus SW feedbacks - are relatively weak at that time of year. For example, Supplementary Figs. 4 and 5 show results analogous to Fig. 3 but for variations in the SAM during July and August. The sea-ice anomalies correlated with July variations in the SAM are dominated by positive anomalies north of the Amundsen Sea and to the east of the Weddell Sea, consistent with the overlying northward component of the wind anomalies, whereas the sea-ice anomalies associated with August variations in the SAM are more varied, with areas of positive and negative anomalies of similar amplitude. In both cases, the sea-ice anomalies are marked by relatively weak clear-sky SW flux anomalies during the following months (compare Supplementary Figs. 4e, f and 5e, f with Fig. 3e, f). As noted earlier (Fig. 2b), results based on months later in the spring (e.g., October and November) are marked by weak hemispheric mean sea-ice anomalies. The weak SIA anomalies arise since the regions of positive and negative sea-ice anomalies largely cancel at this time of year due to regional differences in the pattern of wind anomalies.

The key role of the SAM during the seasonal sea-ice maximum

The persistence of the circulation-induced sea-ice anomalies from one month to the next suggests that circulation anomalies during the sea-ice maximum and—to a lesser degree—the sea-ice minimum have a notable impact on annual mean changes in SIA. The top panel in Fig. 5 shows the regression of annual-mean SIA anomalies onto the SAM as a function of month, where the annual-mean SIA anomalies are formed by averaging SIA over the 12 consecutive months starting from the base month of the regression. For example, the September bar in Fig. 5a is found by regressing SIA averaged over September–August (of the following year) onto September values of the SAM index.

As expected from Fig. 2b, the positive polarity of the SAM leads to increases in annual-mean SIA following the sea-ice minimum but decreases following the sea-ice maximum. The influence of the SAM on year-round SIA is particularly notable following September anomalies in the atmospheric circulation. In terms of variance explained, circulation anomalies during the sea-ice maximum dominate the influence of the SAM on annual mean sea ice: Variations in the SAM during September explain over 30% of the annual-mean variance in SIA, whereas variations in the SAM during other months explains only a small fraction of the year-to-year variance (Supplementary Fig. 6).

The contribution of September variations in the SAM to year-round values of SIA is also visually apparent when the time series of SIA are discretized by year (Fig. 5b). Here, each line shows monthly-mean SIA anomalies for all calendar years starting in September. The colors assigned to each line correspond to the September values of the SAM for that year. To simplify the figure, only years that had a September SAM value exceeding ±1 standard deviation are shown (results including all years are shown in Supplementary Fig. 7). There is a clear correspondence between years that had large positive SIA anomalies and years that had large negative September SAM indices, and vice versa. Years that had particularly large positive or negative SIA anomalies are labeled and exhibit marked correspondence to September values of the SAM. Importantly, years with large September SAM values had substantial SIA anomalies that not only persisted during the spring but throughout the year, consistent with results shown in Figs. 2b, 5a.

As noted in the Introduction, the SAM is significantly correlated with variations in ENSO. However, the most prominent linkages between the SAM and ENSO are limited to the summer months[53], whereas the most prominent contribution of the SAM to hemispheric mean sea ice arises following the sea-ice maximum. Supplementary Fig. 8 shows Fig. 5a reproduced using the Niño3.4 index obtained from the National Oceanic and Atmospheric Administration (NOAA) Climate Prediction Center (Methods). The contribution of ENSO to annual-mean changes in SIA is clearly much smaller than that associated with the SAM, not only following September, but following other months of the year as well (compare Fig. 5a with Supplementary Fig. 8). A more detailed analysis of the signature of ENSO in hemispheric-mean SIA is beyond the scope of the current study.

The linkages between variations in the SAM during the sea-ice maximum and annual mean changes in SH-mean SIA have implications for understanding the large losses in SIA over the past decade. Figure 6 shows September values of the SAM index (gray) superposed on SIA during alternating subsequent months (black). That is: The gray lines in all rows show September values of the SAM index; the black lines show SIA for the indicated months (months not shown in Fig. 6 are shown in Supplementary Fig. 9). The time series are standardized, and the SAM index is inverted so that negative values of the index indicate stronger than normal circumpolar westerlies, and vice versa. There is a clear visual relationship between September values of the SAM index and monthly SIA, not only for SIA values during September, but for SIA values during subsequent months as well.

The linkages between September values of the SAM and SIA are particularly prominent over the past decade. The most notable exception arises in 2023, when sea-ice variability appears to follow variations in the SAM during the summer and autumn months, but not during the spring months of September–November (see also ref. 36). It is worth noting that the key features of the seasonally-varying relationships between the SAM and SIA are reproducible in analyses limited to the period prior to the recent losses. For example, Supplementary Fig. 10 shows the same results as Figs. 2b, 5a but for the period 1979–2015. Variations in the SAM during the sea-ice maximum have played an increasingly large role in annual-mean SIA over the past decade (compare Fig. 5a and Supplementary Fig. 10b), but the general pattern of the seasonally-varying relationships between the SAM and SIA are recovered in analyses based on both the full and earlier periods of record.

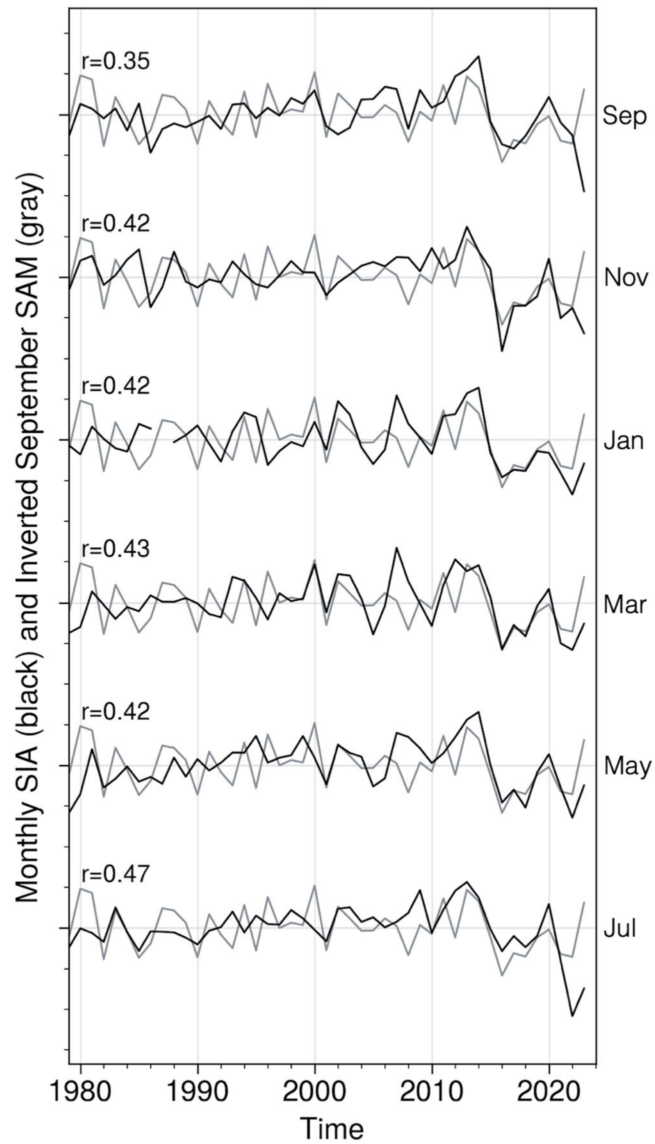

Fig. 6 | Inverted September values of the Southern Annular Mode index and monthly sea-ice area anomalies. Time series of inverted and standardized September values of the Southern Annular Moe (SAM) index (gray) and standardized values of sea-ice area (SIA) anomalies as a function of month (black). That is: Each row shows the same September SAM index time series superposed on standardized values of SIA for the indicated months. The SAM index time series is inverted for the purpose of illustration. SIA time series for months January, March, May, and July are shifted by 1 year so that they align with the SAM index time series during the previous September. The correlation coefficients between each month of SIA and the inverted September SAM are labeled above each times series pair. All data are detrended with respect to the long-term mean climatology. Missing data in the January time series is explained in the Methods section. SIA months shown are chosen at 2-month intervals.

Reproducibility in a climate model

We close the results by exploring the ability of the Community Earth System Model Version 2[70] (CESM2) climate model to reproduce the observed relationships. Figure 7 shows results analogous to Fig. 2b for numerical output from CESM2 run under the Coupled Model Intercomparison Project Phase 6 historical and SSP5-8.5 forcings. During the 20th century (Fig. 7a, b), there is a clear positive correlation between the SAM and SIA during the sea-ice maximum and a clear negative correlation during the sea-ice minimum. As is the case in the observations, the linkages between the SAM and SIA during the sea-ice maximum exhibit more persistence than those during the sea-ice minimum. The simulated linkages have slightly weaker amplitudes compared to observations and peak at slightly different lags (note the colorbar range differences between Fig. 2b and Fig. 7a, b). During the 21st century (Fig. 7c, d), the linkages become increasingly weak, consistent with predicted decreases in sea-ice coverage (Fig. 7e). The broad

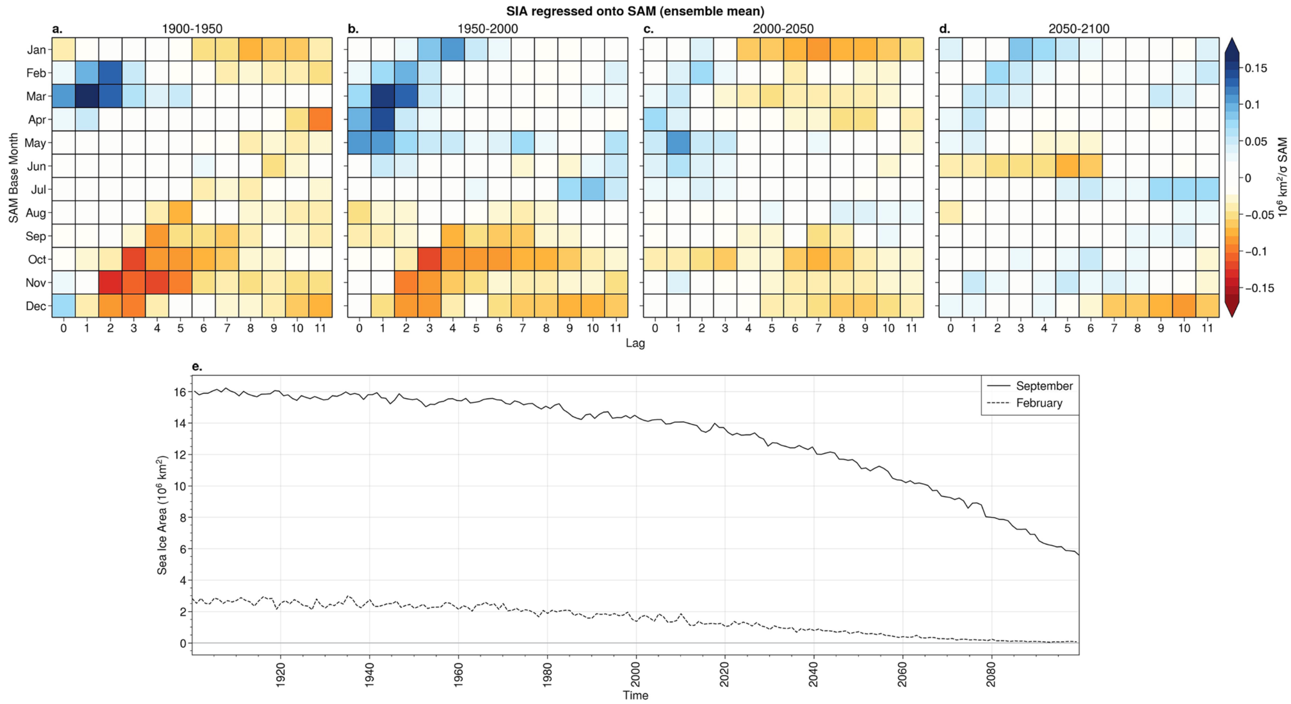

Fig. 7 | The relationship between sea-ice area and the Southern Annular Mode in CESM2. a–d As in Fig. 2b but for results based on ensemble mean output from CESM2 for the periods indicated. Results are formed for individual ensemble members and then averaged over all members. All output is detrended over the indicated periods. **e** Time series of September and February sea-ice area (SIA). SIA used in time series is neither detrended or deseasonalized. Output from 1900 to 2015 is derived from the historical simulation; output from 2015 to 2100 is derived from the SSP5-8.5 simulation. See the main text and "Methods" for details.

similarities between the observed and simulated seasonally-varying relationships during the historical period are encouraging given known biases in model representations of the linkages between the atmospheric circulation and Antarctic sea ice[71,72]. Future changes in the linkages between the SAM and sea-ice extent were also explored in Morioka et al.[73], who found stronger linkages as anthropogenic forcing increases. However, their results are primarily based on annual-mean and contemporaneous correlations, which highlights the importance of the seasonally-varying lagged analysis applied here.

Discussion

Antarctic SIA has exhibited marked declines over the past decade. Several previous studies have probed the role of the atmosphere on the initial declines in sea ice in 2016[31,34,37,39,74], but the sustained losses over the past decade have been primarily linked to ocean warming[34–38,61]. The SAM, in particular, is thought to have played a largely negligible role in the decreases in SH-mean SIA over the past decade[36,44].

The results shown here highlight a key but seemingly overlooked contribution of the SAM to recent changes in SIA. The linkages arise not from the contemporaneous relationships between the SAM and SH-mean SIA, but rather from the marked persistence of sea-ice anomalies induced by the SAM during the sea-ice maximum centered around September. The central findings include the following:

1. The linkages between the SAM and SH-mean SIA vary in both amplitude and sign from one season to the next (Fig. 2b). The most prominent relationships between the SAM and SH-mean SIA arise during the sea-ice maximum and sea-ice minimum: Positive anomalies in the SAM are associated with hemispherically-averaged increases in SH sea ice during the sea-ice minimum, but hemispherically-averaged decreases during the sea-ice maximum.
2. Following the sea-ice minimum, SAM-induced anomalies in sea-ice decay after roughly ~4 months. But following the sea-ice maximum, SAM-induced anomalies in sea ice persist for up to a year. As such, SAM-induced anomalies in sea ice during the sea-ice maximum have an outsized influence on annual-mean SIA. The large persistence in SAM-induced sea-ice anomalies following the sea-ice maximum is consistent with spring/summer feedbacks from both the SW clear-sky fluxes and potentially changes in ocean heat content (Figs. 3 and 4).
3. A notable component of the recent declines in SH-mean SIA is consistent with large variations in the SAM during the late winter/early spring season (Figs. 5b, 6).

The results shown here highlight the key role of the SAM during the sea-ice maximum in driving year-round changes in SH SIA. We have focused on September since it corresponds to (a) the central month of the sea-ice maximum (Fig. 2c), (b) the month during which the SAM exhibited particularly large variability over the past decade (Fig. 6c) and (c) the time of year when the SAM projects onto prominent persistence in SIA (Fig. 2b). It is unclear what gives rise to the weaker relationships between the SAM and SIA prior to 2015 (Supplementary Fig. 10). Potential factors include weaker upper ocean warming prior to 2015, smaller amplitude variations in the SAM, and differences in the mean distribution of sea-ice thickness or concentration.

What physical processes underlie the large and unprecedented variations in the SAM during September in the mid 2010s? Prior to 2016, the SAM exhibited large amplitude anomalies during the cold season months and late spring, but did not exhibit notable anomalies during September. The large amplitude of the SAM during September 2016 and the subsequent decrease in the index through 2017 are unmatched in the historical record (Fig. 6). The variations arise too early in the year to be traced to stratospheric ozone depletion (e.g., ref. 44), and they are not coincident with large anomalies in the SH stratospheric vortex. The unusual variations in the SAM during the sea-ice maximum during the mid-late 2010s may have arisen from a variety of processes, including, for example, atmosphere/ocean interactions, coupling with the stratosphere, the remote response to tropical variability, or simply internal variability in the extratropical atmosphere. The relative contributions of various physical processes to variations in the SAM during the sea-ice maximum remain to be determined.

Methods

Observational, reanalysis, and satellite data

Monthly sea-ice concentration data are from the National Oceanic and Atmospheric Administration/ National Snow and Ice Data Center (NOAA/ NSIDC) Climate Data Record of Passive Microwave Sea Ice Concentration, Version 4[75], and the Near-Real-Time NOAA/NSIDC Climate Data Record of Passive Microwave Sea Ice Concentration, Version 2[76] and has a spatial resolution of 25 × 25 km. The near-real-time sea-ice concentration data are used from January 2024 to July 2024 to provide a continuous record from January 1979 to July 2024, except for December 1987 and January 1988, where there are missing data due to satellite retrieval issues. The sea-ice concentration is reported as the fraction of each grid cell that is covered by sea ice. The time series of SH-mean SIA was found by first multiplying the gridded sea-ice concentration data during each month by the area represented by each grid box, and then summing the resulting values over the SH. Similar results are derived using sea-ice extent, i.e., the area-integral of grid cells with sea-ice concentration greater than 15%.

Monthly mean values of the SAM index are from the NOAA Climate Prediction Center (CPC), where they are calculated by projecting the 700 mb height anomalies poleward of 20°S onto the leading Empirical Orthogonal Function analysis of 700 mb height, then normalized by the standard deviation of the monthly index for the 1979–2000 base period[77]. Monthly mean values of the Niño3.4 index are also obtained from the NOAA CPC. Monthly 10-m wind data is taken from European Centre for Medium-Range Weather Forecasts Reanalysis v5 (ERA5) monthly averaged data on single levels dataset and has a horizontal resolution of 0.25° × 0.25°[78]. The SAM index and wind data cover the period from January 1979 to July 2024.

Surface SW and LW clear-sky radiative flux and CRE data are from the CERES Edition 4.2 Energy Balanced and Filled (EBAF) data product[66]. This monthly data covers the period from March 2000 to July 2024. Fluxes are positive when energy is deposited into the surface and the CRE effect is defined as all-sky flux minus clear-sky flux. The horizontal resolution is 1° × 1°. The CERES product for these variables is used in lieu of a reanalysis product because of the known uncertainty of reanalysis radiative fluxes, especially prior to 2000. Past work has shown that moisture and energy budgets in ERA5 experience spurious trends prior to 2000[79]. Additionally, in the Antarctic, ERA5 has been shown to have biases in mixed-phase clouds that could impact radiative fluxes[80].

Observational SST data are from the Hadley Centre Sea Ice and Sea Surface Temperature (HadISST) dataset[68]. HadISST provides a monthly globally complete sea ice and SST dataset on a 1° × 1° grid starting from 1871. We use the period from January 1979 to July 2024 to align with the availability of other datasets used. The HadISST dataset sets SST values to −1.8 °C for areas with >90% sea-ice concentration, and to NaN for areas with 100% sea-ice concentration.

Model output

Modeled monthly mean sea-ice concentration and geopotential height at 700 mb are from the Coupled Model Intercomparison Project Phase 6 historical and SSP5-8.5 simulations run on CESM2[70]. The SSP5-8.5 scenario is the fossil-fuel development scenario with an additional radiative forcing of 8.5 W/m^2 by 2100 and represents the scenario with very high greenhouse gas emissions[81]. The historical period simulations have 11 ensemble members, and the SSP5-8.5 simulations have three ensemble members. Only the three common ensemble members between the historical and SSP5-8.5 simulations are used to create a continuous record over the period 1900–2100. All simulations have a nominal horizontal resolution 1.25° in longitude and 0.9° in latitude and are run on the Community Atmosphere Model Version 6 (CAM6) with 32 vertical levels and a model top at 2.26 hPa[70]. Modeled monthly mean SAM indices are calculated using the 700 mb geopotential height anomalies, using the same procedure as used by the NOAA CPC for observed SAM indices, as described above. Analysis performed on this model output follows the same process as the observationally-constrained data, with the seasonal cycle removed and all data detrended before analysis.

Analysis methods

Unless otherwise noted, the long-term linear trend and mean seasonal cycle are removed from all data prior to the analyses. The long-term linear trend is calculated across the entire 1979–2024 period for all variables except for the CERES radiative flux data. We emphasize that similar results are derived if the data are not detrended and if they are detrended with a base period of 1979–2015; the period of sea-ice increases (Supplementary Fig. 11). As noted in the text, the broad structure of the results is also reproducible in data restricted to the 1979–2015 epoch (Supplementary Fig. 10). For the CERES radiative flux data, the base period is March 2000–2024 due to data availability. Regression coefficients are calculated as

$$\beta = \frac{\overline{x'y'}}{\overline{x'^2}} \tag{1}$$

where overbars denote the time mean and primes denote departures from the long-term time mean. For all regressions, the independent variable, x, is standardized. Correlation coefficients are computed as

$$r = \frac{\overline{x'y'}}{\sigma_x \sigma_y} \tag{2}$$

where

$$\sigma_x = \left(\overline{x'^2}\right)^{1/2} \tag{3}$$

The fraction of variance explained is calculated by squaring the correlation coefficient. The statistical significance of regression analyses is computed by calculating the significance of the corresponding correlation coefficients r using a Student's t statistic and assuming the effective sample size N_{eff} is $N_{\mathrm{eff}} = N\frac{1-r_1r_2}{1+r_1r_2}$, where N is the number of time steps, r_1 is the lag-1 autocorrelation of the first time series and r_2 is the lag-1 autocorrelation of the second time series[82].

Reporting Summary

Further information on research design is available in the Nature Portfolio Reporting Summary linked to this article.

Data availability

The NOAA/NSIDC Climate Data Record of Passive Microwave Sea Ice Concentration, Version 4 data can be found at https://nsidc.org/data/g02202/versions/4, and the Near-Real-Time NOAA/NSIDC Climate Data Record of Passive Microwave Sea Ice Concentration, Version 2 data can be found at https://nsidc.org/data/g10016/versions/2. The SAM index data from the NOAA CPC can be found at https://www.cpc.ncep.noaa.gov/products/precip/CWlink/daily_ao_index/aao/aao.shtml. The Niño3.4 index data from the NOAA CPC can be found at https://psl.noaa.gov/data/timeseries/month/Nino34_CPC/. ERA5 data can be found at 10.24381/cds.f17050d7. CERES-EBAF surface flux data can be found at https://ceres.larc.nasa.gov/data/. CESM2 data output can be found at https://cseg.cgd.ucar.edu/experiments/public/. Figures were created using the Python package Proplot https://proplot.readthedocs.io/en/latest/index.html.

Code availability

The code to process the data and create the figures is publicly available at https://doi.org/10.5281/zenodo.16943398[83].

Received: 7 April 2025; Accepted: 11 September 2025;
Published online: 22 October 2025

References

1. Parkinson, C. L. A 40-y record reveals gradual Antarctic sea ice increases followed by decreases at rates far exceeding the rates seen in the Arctic. *Proc. Natl. Acad. Sci.* **116**, 14414–14423 (2019).

2. Raphael, M. N. & Handcock, M. S. A new record minimum for Antarctic sea ice. *Nat. Rev. Earth Environ.* **3**, 215–216 (2022).
3. TurnerJ. Record low Antarctic sea ice cover in February *Geophys. Res. Lett.* **49**, e2022GL098904 (2022).
4. Liu, J., Zhu, Z. & Chen, D. Lowest Antarctic sea ice record broken for the second year in a row. *Ocean-Land-Atmos. Res.* **2**, 0007 (2023).
5. Roach, L. A. & Meier, W. N. Sea ice in 2023. *Nat. Rev. Earth Environ.* **5**, 235–237 (2024).
6. Blanchard-Wrigglesworth E. et al. New perspectives on the enigma of expanding Antarctic sea ice, Eos, **103**, https://doi.org/10.1029/2022EO220076 (2022).
7. Ciasto, L. M., Simpkins, G. R. & England, M. H. Teleconnections between tropical Pacific SST anomalies and extratropical Southern hemisphere climate. *J. Clim.* **28**, 56–65 (2015).
8. Hobbs, W. R., Bindoff, N. L. & Raphael, M. N. New perspectives on observed and simulated Antarctic sea ice extent trends using optimal fingerprinting techniques. *J. Clim.* **28**, 1543–1560 (2015).
9. Meehl, G. A., Arblaster, J. M., Bitz, C. M., Chung, C. T. Y. & Teng, H. Antarctic sea-ice expansion between 2000 and 2014 driven by tropical Pacific decadal climate variability. *Nat. Geosci.* **9**, 590–595 (2016).
10. Li, X. et al. Tropical teleconnection impacts on Antarctic climate changes. *Nat. Rev. Earth Environ.* **2**, 680–698 (2021).
11. Chung, E.-S. et al. Antarctic sea-ice expansion and Southern Ocean cooling linked to tropical variability. *Nat. Clim. Chang.* **12**, 461–468 (2022).
12. Bonan, D. B., Dörr, J., Wills, R. C. J., Thompson, A. F. & Årthun, M. Sources of low-frequency variability in observed Antarctic sea ice. *Cryosphere* **18**, 2141–2159 (2024).
13. Fyfe, J. C., Gillett, N. P. & Marshall, G. J. Human influence on extratropical Southern Hemisphere summer precipitation. *Geophys. Res. Lett.* **39**, L23711 (2012).
14. Pauling, A. G., Bitz, C. M., Smith, I. J. & Langhorne, P. J. The response of the Southern Ocean and Antarctic sea ice to freshwater from ice shelves in an Earth System Model. *J. Clim.* **29**, 1655–1672 (2016).
15. Purich, A., England, M. H., Cai, W., Sullivan, A. & Durack, P. J. Impacts of broad-scale surface freshening of the Southern Ocean in a coupled climate model. *J. Clim.* **31**, 2613–2632 (2018).
16. Sadai, S., Condron, A., DeConto, R. & Pollard, D. Future climate response to Antarctic Ice Sheet melt caused by anthropogenic warming. *Sci. Adv.* **6**, eaaz1169 (2020).
17. Rye, C. D. et al. Antarctic glacial melt as a driver of recent Southern Ocean climate trends. *Geophys. Res. Lett.* **47**, e2019GL086892 (2020).
18. Dong, Y., Pauling, A. G., Sadai, S. & Armour, K. C. Antarctic ice-sheet meltwater reduces transient warming and climate sensitivity through the sea-surface temperature pattern effect. *Geophys. Res. Lett.* **49**, e2022GL101249 (2022).
19. Blanchard-Wrigglesworth, E., Roach, L. A., Donohoe, A. & Ding, Q. Impact of winds and Southern Ocean SSTs on Antarctic sea ice trends and variability. *J. Clim.* **34**, 949–965 (2021).
20. Zhang, X., Deser, C. & Sun, L. Is there a tropical response to recent observed Southern Ocean cooling? *Geophys. Res. Lett.* **48**, e2020GL091235 (2021).
21. Sun, S. & Eisenman, I. Observed Antarctic sea ice expansion reproduced in a climate model after correcting biases in sea ice drift velocity. *Nat. Commun.* **12**, 1060 (2021).
22. Turner, J. et al. Non-annular atmospheric circulation change induced by stratospheric ozone depletion and its role in the recent increase of Antarctic sea ice extent. *Geophys. Res. Lett.* **36**, L08502 (2009).
23. Doddridge, E. W. & Marshall, J. Modulation of the seasonal cycle of Antarctic sea ice extent related to the Southern Annular Mode. *Geophys. Res. Lett.* **44**, 9761–9768 (2017).
24. Hall, A. & Visbeck, M. Synchronous variability in the Southern Hemisphere atmosphere, sea ice, and ocean resulting from the Annular Mode. *J. Clim.* **15**, 3043–3057 (2002).
25. Stammerjohn, S. E., Martinson, D. G., Smith, R. C., Yuan, X. & Rind, D. Trends in Antarctic annual sea ice retreat and advance and their relation to El Niño–Southern Oscillation and Southern Annular Mode variability. *J. Geophys. Res. Oceans* **113**, C03S90 (2008).
26. Simpkins, G. R., Ciasto, L. M., Thompson, D. W. J. & England, M. H. Seasonal relationships between large-scale climate variability and Antarctic sea ice concentration. *J. Clim.* **25**, 5451–5469 (2012).
27. Raphael, M. N. & Hobbs, W. The influence of the large-scale atmospheric circulation on Antarctic sea ice during ice advance and retreat seasons. *Geophys. Res. Lett.* **41**, 5037–5045 (2014).
28. Kostov, Y. et al. Fast and slow responses of Southern Ocean sea surface temperature to SAM in coupled climate models. *Clim. Dyn.* **48**, 1595–1609 (2017).
29. Schemm, S. Regional trends in weather systems help explain Antarctic sea ice trends. *Geophys. Res. Lett.* **45**, 7165–7175 (2018).
30. Roach, L. A. et al. Winds and meltwater together lead to Southern Ocean surface cooling and sea ice expansion. *Geophys. Res. Lett.* **50**, e2023GL105948 (2023).
31. Schlosser, E., Haumann, F. A. & Raphael, M. N. Atmospheric influences on the anomalous 2016 Antarctic sea ice decay. *Cryosphere* **12**, 1103–1119 (2018).
32. Purich, A. & England, M. H. Tropical teleconnections to Antarctic sea ice during austral spring 2016 in coupled pacemaker experiments. *Geophys. Res. Lett.* **46**, 6848–6858 (2019).
33. Wang, G. et al. Compounding tropical and stratospheric forcing of the record low Antarctic sea-ice in 2016. *Nat. Commun.* **10**, 13 (2019).
34. Meehl, G. A. et al. Sustained ocean changes contributed to sudden Antarctic sea ice retreat in late 2016. *Nat. Commun.* **10**, 14 (2019).
35. Zhang, L. et al. The relative role of the subsurface Southern Ocean in driving negative Antarctic Sea ice extent anomalies in 2016–2021. *Commun. Earth Environ.* **3**, 1–9 (2022).
36. Purich, A. & Doddridge, E. W. Record low Antarctic sea ice coverage indicates a new sea ice state. *Commun. Earth Environ.* **4**, 1–9 (2023).
37. Jena, B. et al. Evolution of Antarctic sea ice ahead of the record low annual maximum extent in September 2023. *Geophys. Res. Lett.* **51**, e2023GL107561 (2024).
38. Espinosa, Z. I., Blanchard-Wrigglesworth, E. & Bitz, C. M. Understanding the drivers and predictability of record low Antarctic sea ice in austral winter 2023. *Commun. Earth Environ.* **5**, 1–9 (2024).
39. Turner, J. et al. Unprecedented springtime retreat of Antarctic sea ice in 2016. *Geophys. Res. Lett.* **44**, 6868–6875 (2017).
40. Stuecker, M. F., Bitz, C. M. & Armour, K. C. Conditions leading to the unprecedented low Antarctic sea ice extent during the 2016 austral spring season. *Geophys. Res. Lett.* **44**, 9008–9019 (2017).
41. Yadav, J., Kumar, A. & Mohan, R. Atmospheric precursors to the Antarctic sea ice record low in February 2022. *Environ. Res. Commun.* **4**, 121005 (2022).
42. Thompson, D. W. J. & Wallace, J. M. Annular Modes in the extratropical circulation. Part I: month-to-month variability. *J. Clim.* **13**, 1000–1016 (2000).
43. Ciasto, L. M. & Thompson, D. W. J. Observations of large-scale ocean–atmosphere interaction in the Southern hemisphere. *J. Clim.* **21**, 1244–1259 (2008).
44. Polvani, L. M. et al. Interannual SAM modulation of Antarctic sea ice extent does not account for its long-term trends, pointing to a limited role for ozone depletion. *Geophys. Res. Lett.* **48**, e2021GL094871 (2021).
45. Sigmond, M. & Fyfe, J. C. Has the ozone hole contributed to increased Antarctic sea ice extent? *Geophys. Res. Lett.* **37**, L18502 (2010).

46. Ferreira, D., Marshall, J., Bitz, C. M., Solomon, S. & Plumb, A. Antarctic ocean and sea ice response to ozone depletion: a two-time-scale problem. *J. Clim.* **28**, 1206–1226 (2015).
47. Bitz, C. M. & Polvani, L. M. Antarctic climate response to stratospheric ozone depletion in a fine resolution ocean climate model. *Geophys. Res. Lett.* **39**, L20705 (2012).
48. Dong, Y., Polvani, L. M. & Bonan, D. B. Recent multi-decadal Southern Ocean surface cooling unlikely caused by Southern Annular Mode trends. *Geophys. Res. Lett.* **50**, e2023GL106142 (2023).
49. Thompson, D. W. J. & Solomon, S. Interpretation of recent southern hemisphere climate change. *Science* **296**, 895–899 (2002).
50. Polvani, L. M., Waugh, D. W., Correa, G. J. P. & Son, S.-W. Stratospheric ozone depletion: the main driver of twentieth-century atmospheric circulation changes in the Southern hemisphere. *J. Clim.* **24**, 795–812 (2011).
51. Kushner, P. J., Held, I. M. & Delworth, T. L. Southern hemisphere atmospheric circulation response to global warming. *J. Clim.* **14**, 2238–2249 (2001).
52. Arblaster, J. M. & Meehl, G. A. Contributions of external forcings to Southern annular mode trends. *J. Clim.* **19**, 2896–2905 (2006).
53. L'Heureux, M. L. & Thompson, D. W. J. Observed relationships between the El Niño–Southern oscillation and the extratropical zonal-mean circulation. *J. Clim.* **19**, 276–287 (2006).
54. Marshall, G. J. Trends in the Southern annular mode from observations and reanalyses. *J. Clim.* **16**, 4134–4143 (2003).
55. Thompson, D. W. J. et al. Signatures of the Antarctic ozone hole in Southern Hemisphere surface climate change. *Nat. Geosci.* **4**, 741–749 (2011).
56. Fogt, R. L. & Marshall, G. J. The Southern annular mode: variability, trends, and climate impacts across the Southern hemisphere. *WIREs Clim. Change* **11**, e652 (2020).
57. Holland, M. M., Blanchard-Wrigglesworth, E., Kay, J. & Vavrus, S. Initial-value predictability of Antarctic sea ice in the Community Climate System Model 3. *Geophys. Res. Lett.* **40**, 2121–2124 (2013).
58. Ordoñez, A. C., Bitz, C. M. & Blanchard-Wrigglesworth, E. Processes controlling Arctic and Antarctic sea ice predictability in the Community Earth System Model. *J. Clim.* **31**, 9771–9786 (2018).
59. Marchi, S. et al. Reemergence of Antarctic sea ice predictability and its link to deep ocean mixing in global climate models. *Clim. Dyn.* **52**, 2775–2797 (2019).
60. Libera, S., Hobbs, W., Klocker, A., Meyer, A. & Matear, R. Ocean-sea ice processes and their role in multi-month predictability of Antarctic sea ice. *Geophys. Res. Lett.* **49**, e2021GL097047 (2022).
61. Hobbs, W. et al. Observational evidence for a regime shift in summer Antarctic sea ice. *J. Clim.* **37**, 2263–2275 (2024).
62. Blanchard-Wrigglesworth, E., Armour, K. C., Bitz, C. M. & DeWeaver, E. Persistence and inherent predictability of Arctic sea ice in a GCM ensemble and observations. *J. Clim.* **24**, 231–250 (2011).
63. Holland, M. M., Landrum, L., Raphael, M. & Stammerjohn, S. Springtime winds drive Ross Sea ice variability and change in the following autumn. *Nat. Commun.* **8**, 731 (2017).
64. Holland, M. M., Landrum, L., Raphael, M. N. & Kwok, R. The regional, seasonal, and lagged influence of the Amundsen Sea low on Antarctic sea ice. *Geophys. Res. Lett.* **45**, 227–11,234 (2018).
65. Alexander, M. A., Deser, C. & Timlin, M. S. The reemergence of SST anomalies in the North Pacific Ocean. *J. Clim.* **12**, 2419–2433 (1999).
66. Kato, S. et al. Surface irradiances of edition 4.0 clouds and the Earth's radiant energy system (CERES) energy balanced and filled (EBAF) data product. *J. Clim.* **31**, 4501–4527 (2018).
67. Kay, J. E. & Gettelman, A. Cloud influence on and response to seasonal Arctic sea ice loss. *J. Geophys. Res. Atmos.* **114**, D18204 (2009).
68. Rayner, N. A. et al. Global analyses of sea surface temperature, sea ice, and night marine air temperature since the late nineteenth century. *J. Geophys. Res. Atmos.* **108**, 4407 (2003).
69. Roemmich, D. & Gilson, J. The 2004–2008 mean and annual cycle of temperature, salinity, and steric height in the global ocean from the Argo Program. *Prog. Oceanogr.* **82**, 81–100 (2009).
70. Danabasoglu, G. et al. The community Earth system model version 2 (CESM2). *J. Adv. Model. Earth Syst.* **12**, e2019MS001916 (2020).
71. Roach, L. A. et al. Antarctic sea ice area in CMIP6. *Geophys. Res. Lett.* **47**, e2019GL086729 (2020).
72. Wills, R. C. J., Dong, Y., Proistosecu, C., Armour, K. C. & Battisti, D. S. Systematic climate model biases in the large-scale patterns of recent sea-surface temperature and sea-level pressure change. *Geophys. Res. Lett.* **49**, e2022GL100011 (2022).
73. Morioka, Y. et al. Role of anthropogenic forcing in Antarctic sea ice variability simulated in climate models. *Nat. Commun.* **15**, 10511 (2024).
74. Ionita, M. Large-scale drivers of the exceptionally low winter Antarctic sea ice extent in 2023. *Front. Earth Sci*. **12**, 1333706 (2024).
75. Meier, W. N. et al. NOAA/NSIDC Climate Data Record of Passive Microwave Sea Ice Concentration. (G02202, Version 4). https://doi.org/10.7265/efmz-2t65.
76. Meier, W. N. et al. Near-Real-Time NOAA/NSIDC Climate Data Record of Passive Microwave Sea Ice Concentration. (G10016, Version 2). https://doi.org/10.7265/tgam-yv28.
77. Mo, K. C. Relationships between low-frequency variability in the Southern hemisphere and sea surface temperature anomalies. *J. Clim.* **13**, 3599–3610 (2000).
78. Hersbach, H. et al. The ERA5 global reanalysis. *Q. J. R. Meteorol. Soc.* **146**, 1999–2049 (2020).
79. Mayer, J., Mayer, M. & Haimberger, L. Consistency and homogeneity of atmospheric energy, moisture, and mass budgets in ERA5. *J. Clim.* **34**, 3955–3974 (2021).
80. Silber, I. et al. 2019: Cloud influence on ERA5 and AMPS surface downwelling longwave radiation biases in West Antarctica. *J. Clim.* **32**, 7935–7949 (2019).
81. Riahi, K. et al. The shared socioeconomic pathways and their energy, land use, and greenhouse gas emissions implications: an overview. *Glob. Environ. Change* **42**, 153–168 (2017).
82. Bretherton, C. S., Widmann, M., Dymnikov, V. P., Wallace, J. M. & Bladé, I. The effective number of spatial degrees of freedom of a time-varying field. *J. Clim.* **12**, 1990–2009 (1999).
83. Boehm, C. Code for Boehm et al. 2025. *Zenodo*. https://doi.org/10.5281/zenodo.16943398 (2025).

Acknowledgements

We thank Kyle Clem, Caroline Holmes, and the anonymous reviewer for their helpful and insightful comments on the paper. We thank Lantao Sun for his guidance in accessing and using CESM2 output. C.L.B. is supported by the NSF CLD Program AGS- 2055121; D.W.J.T. is supported by the NSF CLD Program under AGS-2116186 and AGS- 2055121, NSF GEO-NERC 5320798, and the National Aeronautics and Space Administration (NASA) under 80NSSC23K0113. E.B.W. is supported by NSF OPP 2213988 and NSF OPP 2233421.

Author contributions

C.L.B., D.W.J.T., and E.B.W. conceived the study and wrote the paper. C.L.B. performed the analysis and prepared the figures.

Competing interests

The authors declare no competing interests.

Additional information

Supplementary information The online version contains supplementary material available at https://doi.org/10.1038/s43247-025-02792-2.

Correspondence and requests for materials should be addressed to Chloe L. Boehm.

Peer review information *Communications Earth & Environment* thanks Caroline Holmes, Ryan Fogt and Kyle Clem, reviewer(s) for their contribution to the peer review of this work. Primary Handling Editors: Seung-Ki Min and Alireza Bahadori. A peer review file is available.